



This is a repository copy of *Experimental investigation of cross-sectional bending capacity of cold-formed steel channels subject to local-distortional buckling interaction*.

White Rose Research Online URL for this paper:
<http://eprints.whiterose.ac.uk/144788/>

Version: Accepted Version

Article:

Ye, J., Meza, F.J., Hajirasouliha, I. orcid.org/0000-0003-2597-8200 et al. (3 more authors) (2019) Experimental investigation of cross-sectional bending capacity of cold-formed steel channels subject to local-distortional buckling interaction. *Journal of Structural Engineering*, 145 (7). 04019064. ISSN 0733-9445

[https://doi.org/10.1061/\(ASCE\)ST.1943-541X.0002344](https://doi.org/10.1061/(ASCE)ST.1943-541X.0002344)

This material may be downloaded for personal use only. Any other use requires prior permission of the American Society of Civil Engineers. This material may be found at [https://doi.org/10.1061/\(ASCE\)ST.1943-541X.0002344](https://doi.org/10.1061/(ASCE)ST.1943-541X.0002344)

Reuse

Items deposited in White Rose Research Online are protected by copyright, with all rights reserved unless indicated otherwise. They may be downloaded and/or printed for private study, or other acts as permitted by national copyright laws. The publisher or other rights holders may allow further reproduction and re-use of the full text version. This is indicated by the licence information on the White Rose Research Online record for the item.

Takedown

If you consider content in White Rose Research Online to be in breach of UK law, please notify us by emailing eprints@whiterose.ac.uk including the URL of the record and the reason for the withdrawal request.



eprints@whiterose.ac.uk
<https://eprints.whiterose.ac.uk/>

Experimental investigation of the local and distortional buckling interaction and deflection of CFS back-to-back channel sections

Jun Ye ^{a,b}, Francisco J. Meza ^a, Iman Hajirasouliha ^a, Jurgen Becque ^a, Paul Shepherd ^b and Kypros Pilakoutas ^a

^a Department of Civil and Structural Engineering, The University of Sheffield, Sheffield, UK

^b Department of Architecture and Civil Engineering, University of Bath, Bath, UK

Emails: j.ye@bath.ac.uk

Abstract: This paper describes an experimental programme carried out at the University of Sheffield to investigate the interaction between local and distortional buckling in cold-formed steel (CFS) bolted back-to-back beams, assembled from lipped channel sections. The results are used to verify the accuracy of the current design procedures in Eurocode 3, as well as to evaluate the effectiveness of a previously proposed optimisation methodology for CFS members in bending. A total of six tests on back-to-back beams, including three different cross-sectional geometries, were conducted in a four-point bending configuration with simply supported boundary conditions. All beams were manufactured using steel plate of the same coil width and thickness and failed due to interaction between local and distortional buckling. The geometric imperfections of the individual channels, as well as those of the back-to-back specimens, were recorded using a specially designed precision measurement rig. Tensile coupons were also extracted from both the flat and corner regions of the cross-sections to determine the material properties. The results show that Eurocode 3 is accurate in predicting the strength of back-to-back channel beams subject to local/distortional buckling. It was also confirmed that optimised CFS beams exhibited a capacity up to 18% higher than the standard channel section with the same amount of material. It is shown that using reduced cross-sectional properties to calculate deflections leads to a slight overestimation of the deflections at a serviceability load level, whilst linear elastic full cross-sectional properties consistently underestimate deflections.

Keywords: Back-to-back beam; Experiment; Cold-formed steel; Local buckling; Distortional buckling; Deflections

1 Introduction

Cold-formed steel (CFS) beams are used in a wide range of applications, particularly in secondary load-carrying members such as roof purlins, mezzanine floors, storage racks and wall girts. In recent years, however, CFS beams are increasingly used as primary structural elements in low- to mid-rise

multi-storey buildings [1] and CFS portal frames with short to intermediate spans [2, 3]. Compared to their hot-rolled counterparts, CFS thin-walled members possess a number of advantages, such as a larger strength-to-weight ratio, higher flexibility in cross-sectional shapes, a relatively straightforward fabrication and manufacturing process and the ease of transportation and installation.

On the other hand, the limited wall thickness of CFS members results in their ultimate capacity being governed by instabilities such as local, distortional and global buckling, whilst possible interactions between these buckling modes also have to be considered. In addition, as a result of the manufacturing process, CFS members tend to have a single or rotational symmetry in cross-section, while double symmetry is difficult to obtain. This means that in most cases it is difficult (or practically impossible) to apply the load at the shear center of the cross-section. This results in additional torsion in these members, while their open cross-section only affords low torsional rigidity. However, doubly-symmetric cross-sections can easily be obtained by connecting two single sections together, thereby restraining (or even eliminating) certain instabilities and increasing the ultimate capacity of the member.

Experimental investigations into the ultimate strength have been conducted on CFS single beam section with simple and complex edge stiffeners [4-6]. CFS back-to-back sections, which are made from connecting two channel sections, are able to provide more torsional rigidity. In order to study the flexural behaviour of cold-formed steel channel beams, experiments were conducted by Hsu and Chi [7] on back-to-back CFS beams under the monotonic and cyclic load. An experimental and numerical study on the behaviour CFS built-up beam members was conducted by Laím et al. [8], which found that the behaviour of those beams was significantly affected by the distribution of screws and the interaction of local/distortional and lateral-torsional buckling. In some of the specimens without load transfer plates, web crippling occurred due to load concentration, as is the failure phenomena indicated in [9]. Manikandan et al. [10] studied the bending behaviour of innovative CFS back-to-back channel sections with folded flange and complex edge stiffeners, both experimentally and numerically, and showed that sections with complex edge stiffeners and folded flanges had the maximum bending strength. Wang and Young [11] investigated the behaviour of simply supported built-up section beams with different web intermediate stiffeners under four-point bending and three-point bending tests. Using validated and extended numerical study [12], the behaviour and design rule for built-up section beam were presented. Poologanathan and Mahen [13] studied the shear behaviour and strength of an innovative LiteSteel Beam section with box flanges, the specimens were tested in both a single and back-to-back configuration and it was found that significant improvement of shear strength was obtained compared to conventional lipped channel.

In past optimisation studies, the strength capacities of selected prototypes were conventionally determined using the conventional “effective width method” [14-16]. Karim [17] optimised hat, I- and Z-shapes cross-sections using the neutral network method. Lee et al. [18, 19] investigated the optimum design of channel beams and columns by using the micro genetic algorithms. Tian and Lu [20] investigated the minimum weight of the cold-formed C-channel sections with and without lips with a fix coil width subjected to a prescribed axial compressive load. The “direct strength method” (DSM) [15] were later used for free-form optimisation of CFS elements. Leng et al. [23] combined the DSM with the gradient-based steepest descent method as well as genetic and simulated annealing algorithms to obtain CFS sections with maximum capacity. Leng et al. [24] extended this method by incorporating constraints on the number of bent rollers, which resulted in reduced manufacturing costs. Madeira et al. [25] conducted multi-objective optimisation of CFS elements in compression. The local-global buckling strength and distortional buckling strength were taken as two objectives. Trade-off Pareto optimal fronts were provided for symmetric and anti-symmetric cross-section shapes.

More recently, CFS channel columns with intermediate V-shaped web stiffeners and return lip stiffeners were tested between pin-ended boundary conditions by Wang et al. [26]. The results of the investigation indicated that a combination of web and edge stiffeners have the potential to increase the ultimate strength of CFS channel columns by up to 70%. These results highlight the scope for optimisation research on CFS structures and the potential benefits which can be gained from developing cross-sectional shapes with improved structural capacity. An aspect of optimisation was therefore included in the research presented in this paper. However, the available tests on CFS sections were generally designed for the development of design guidance for CFS specimens, while no comparisons between standard and optimised sections were presented. Therefore, newly proposed cross-sectional shapes are not usually optimised on the basis of detailed experimental validation and calibration, and a direct comparison of optimisation results with actual experiments on strength and deflections of CFS beams has not been carried out to date.

This paper presents an experimental programme comprised of six back-to-back CFS beams, each assembled from two lipped channels in a back-to-back configuration. The built-up specimens were tested in four-point bending and were designed to fail dominantly by interaction of local and distortional buckling in the constant moment region. It is noted that this experimental programme is part of a wider study into the optimisation of CFS members [27, 28], which is why all cross-sections in the test programme were manufactured using the same coil width and thickness, keeping the amount of material constant across the test specimen range. However, the experimental results are

here presented independently of their wider context, as the results by themselves provide valuable data about the interactive buckling behaviour of CFS back-to-back channel beams. A comparison of the experimental ultimate capacities and deflections at serviceability load level with those predicted by the Eurocode 3 design guidelines [29-31] is also presented.

2 Section geometry and labelling

In the design of the test specimens an optimisation framework was employed which was previously developed by the authors [27, 28] for the purpose of generating more efficient CFS elements in bending. The proposed optimisation framework predicts the ultimate capacity of CFS elements according to EN 1993-1-3 (2006). The total developed length of the cross-section (coil width) and the thickness (and consequently the total amount of material) were kept constant in the optimisation procedures. In the research by Ye et al. [27, 28], the framework was successfully applied to obtain optimum CFS beam sections within Eurocode 3 design requirements and manufacturing and construction constraints. In order to apply the framework to design the tested specimens for this paper and to verify the optimisation process, the following objective function needed to be maximized:

$$\max M_{c,Rd} = \chi_{LT} \cdot W_{eff} \cdot f_y \quad (1)$$

subject to:

$$b/t \leq 60, c/t \leq 50, h/t \leq 500 \quad (2)$$

$$0.2 \leq c/b \leq 0.6 \quad (3)$$

$$b \geq 50, c \leq 25 \quad (4)$$

$$\Delta < \Delta_{lim} \quad (5)$$

where $M_{c,Rd}$ is the bending capacity, W_{eff} is the effective modulus of the cross-section considering the local/distortional buckling and the inelastic strength reserve of the cross-section (as explained in Section 7). χ_{LT} is the reduction factor taken into account the lateral-torsional buckling and is defined in detail in Section 7. h is the cross-sectional height, and b and c are the flange and lip width, respectively. t is the thickness of the cross-section while f_y is the yield stress of the material used. Eqs.(2) and (3) represent the width-to-thickness ratio limits defined in EC3[30]. Eq.(4) is used to take into account the manufacturing and construction constraints.

Eq.(5) imposes a constraint on the upper limit of deflection $\Delta_{lim}=L/200$ ($L=1200\text{ mm}$ is the beam span) of the CFS beams [32]. A load factor of $1/1.35=0.74$ is used when calculating the deflections Δ using effective cross-section according to Eurocode 3 [29, 30], which means the deflection is obtained by using a moment ratio of $M_s = 0.74M_{c,Rd}$. This is due to the fact that in the ultimate limit state design of CFS beams, the partial factor of 1.35 is used for the dead load while 1.5 is used for the live load. However, the partial factors are 1.0 for serviceability limit state design. A load factor of $1/1.35=0.74$ means a slightly larger deflection will be calculated which can be in the safe side with a slightly lower factor 1.35 used for live load (instead of 1.5). When calculating the deflection, a uniform bending moment is applied at both ends of a simply-supported beam. Whilst these constraints might prevent a global optimum being reached, they illustrate very well the capabilities of the previously proposed optimisation framework [27, 28] to incorporate various practical limitations. During the optimisation process it was found that local/distortional buckling resistance is dominant whilst the effect of lateral-torsional buckling and deflection limits are minor, this is illustrated by the test results presented later.

The back-to-back specimens were assembled using lipped channels with three different cross-sectional geometries. All channels were fabricated by brake pressing a pre-galvanized steel sheet with a width of 415 mm , a nominal thickness of 1.5 mm and a zinc coating of 0.04 mm thickness. The nominal yield stress of the sheet was $f_y=450\text{ MPa}$, as presented in the optimisation framework in Eqs.(1)-(4). The back-to-back beams had a total length of 3300 mm and a distance between the end supports of 3100 mm . M12 zinc-plated bolts, tightened with a constant torque of $15\text{ N}\cdot\text{m}$, were used to connect the individual channel sections through the web, as illustrated in Fig. 1, under the loading points and over the end supports. The bolt holes, with standard bolt hole size of 14 mm , were drilled into the webs of the specimens as shown in Fig.2.

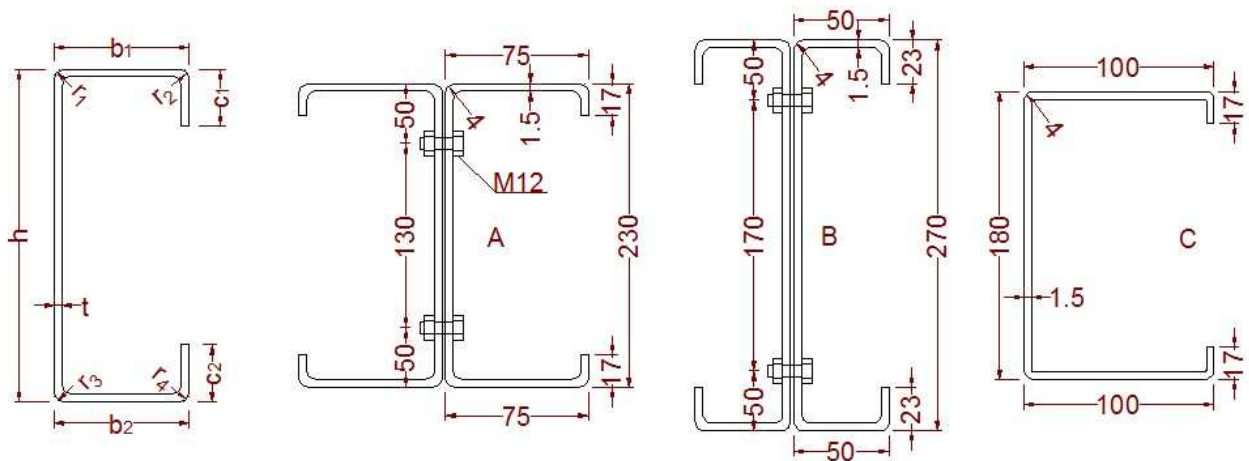


Fig.1 Symbol definitions and nominal cross-sectional dimensions

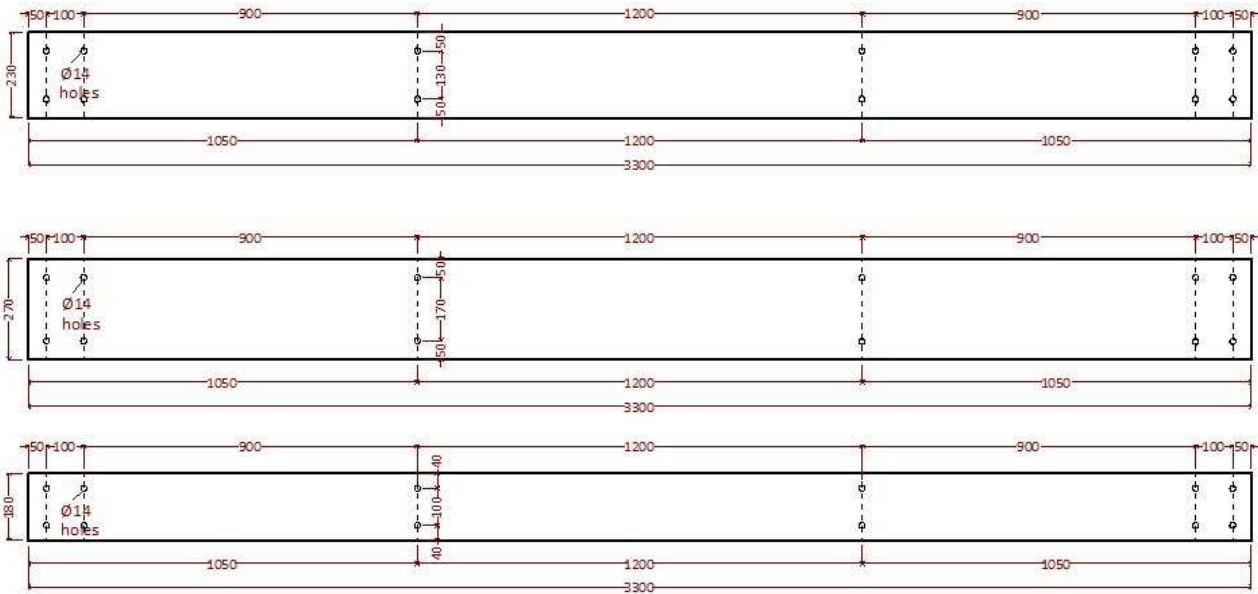


Fig.2 Bolt hole arrangement in the tested beams

Each back-to-back specimen was labelled according to its cross-section, using the letters *A*, *B* or *C* (Fig. 1), followed by the height of the cross-section in mm. As each test was repeated, the numbers 1 and 2 were used to differentiate between the first and second twin specimen. For each back-to-back specimen, the letters ‘*a*’ and ‘*b*’ were used to refer to the individual channels which formed the back-to-back cross-section.

The cross-sectional dimensions of each channel were measured prior to their assemblage. Tables 1-3 list the measured dimensions of the test specimens, using the nomenclature illustrated in Figure 1. All the reported values correspond to outer dimensions and they are the averages of several measurements taken along the length of the channels. The calculated gross cross-sectional moment of inertia of the sections is denoted by I_y and is also listed in Tables 1-3.

Table 1. Measured dimensions of specimens with cross-section A

Specimen	Channel	r (mm)	t (mm)	h (mm)	b_1 (mm)	c_1 (mm)	b_2 (mm)	c_2 (mm)	I_y (mm ⁴)
A230-1	a	3.9	1.563	230.43	75.36	17.44	75.35	16.81	4754469
	b	4.3	1.551	230.35	75.33	17.44	75.33	16.86	4706976
A230-2	a	4.1	1.557	230.52	75.35	16.64	75.35	17.39	4749301
	b	3.7	1.564	230.48	74.90	16.09	74.90	17.25	4733980
Average		4.0	1.559	230.45	75.24	16.90	75.23	17.08	4736182
St. Dev.		0.15	0.01	0.07	0.22	0.66	0.22	0.29	21326

Table 2. Measured dimensions of specimens with cross-section B

Specimen	Channel	r (mm)	t (mm)	h (mm)	b_1 (mm)	c_1 (mm)	b_2 (mm)	c_2 (mm)	I_y (mm ⁴)
B270-1	a	4.1	1.561	269.49	50.19	24.70	50.10	23.79	5807349
	b	4.0	1.565	270.59	51.33	23.24	49.71	23.47	5857038
B270-2	a	4.2	1.555	270.43	50.95	23.01	49.91	23.50	5793464
	b	4.1	1.546	270.55	51.34	23.29	50.25	22.84	5820003
Average		4.1	1.557	270.30	51.00	23.60	50.00	23.40	5819463
St. Dev.		0.08	0.01	0.52	0.54	0.77	0.23	0.40	27294

Table 3. Measured dimensions of specimens with cross-section C

Specimen	Channel	r (mm)	t (mm)	h (mm)	b_1 (mm)	c_1 (mm)	b_2 (mm)	c_2 (mm)	I_y (mm ⁴)
C180-1	a	4.1	1.554	180.30	100.41	17.31	100.33	17.06	3250607
	b	3.9	1.567	180.20	100.38	17.53	100.14	16.80	3288756
C180-2	a	3.9	1.559	180.52	100.41	17.46	100.33	17.28	3287688
	b	4.2	1.554	180.41	100.43	17.34	100.32	16.75	3250202
Average		4.0	1.559	180.36	100.41	17.41	100.28	16.97	3269313
St. Dev.		0.15	0.01	0.14	0.02	0.10	0.09	0.25	21839

The software package CUFSM [21], which implements the finite strip method, was modified to be able to extract the individual buckling modes and used to determine the critical elastic buckling moment of each type of cross-section, as shown in Fig. 3. The signature curves were obtained by using the nominal dimensions and thickness for a single channel. It is seen that the local and distortional buckling bending moments of A cross-section series are almost at the same level for all cross-sections listed in Table 1, this indicates that the interaction of local and distortional buckling could happen. For B cross-section series, the local buckling bending moment is critical compared to the distortional buckling bending moment. It is also seen that the local buckling bending moment of C cross-section series significantly exceeds the distortional buckling bending moment. This will result a more critical distortional buckling mode. For all of the sections, the local and distortional buckling moment is always significantly smaller than the yield bending moment. The elastic global buckling moments are also indicated in the diagrams for various beam spans and it is shown that the lateral-torsional buckling is not dominant for all the sections with a span of $L=1200\text{ mm}$.

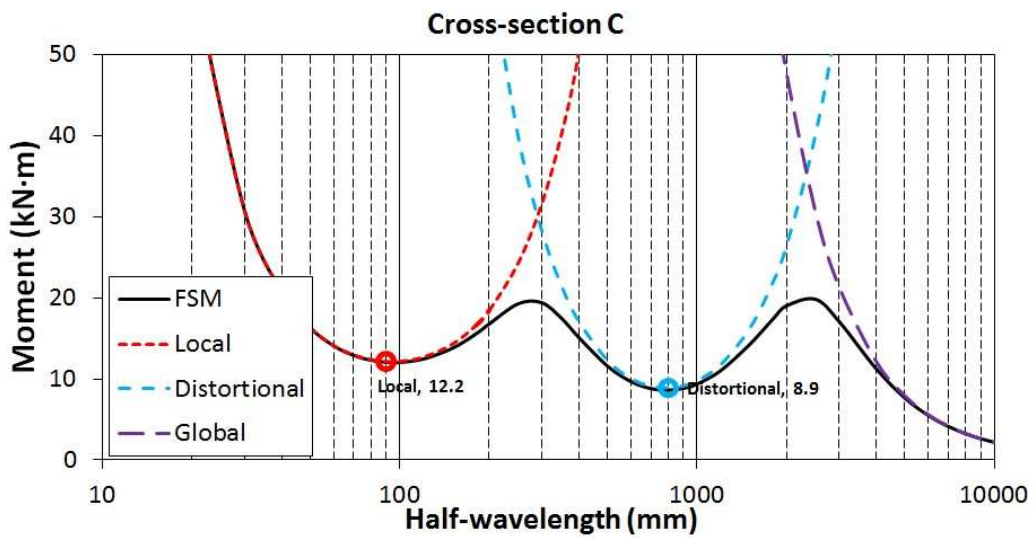
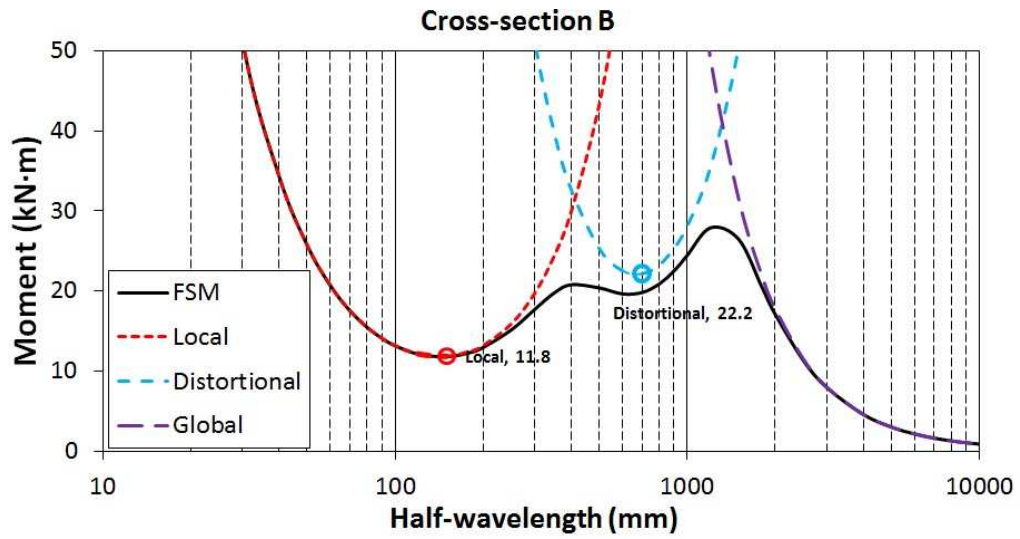
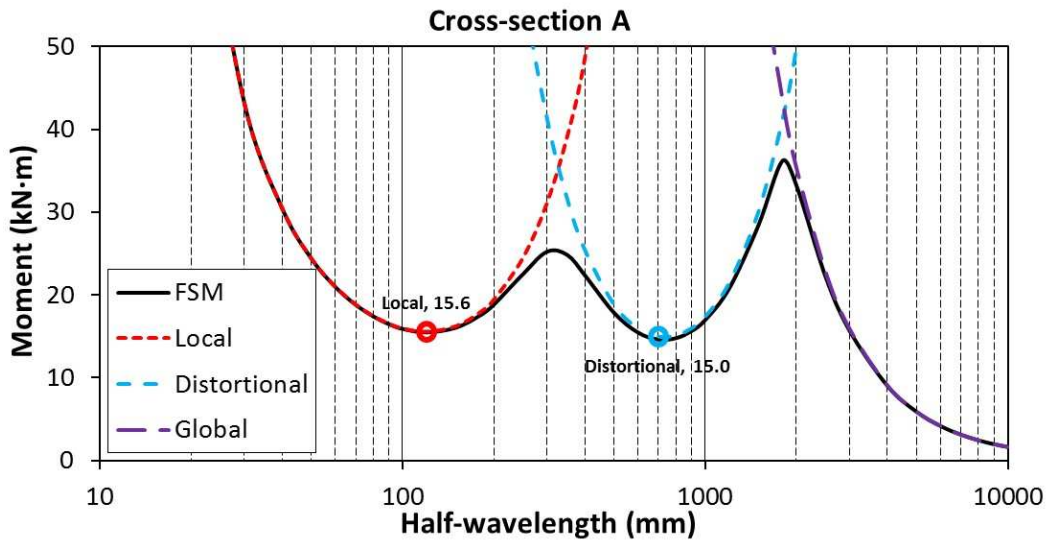


Fig.3 Signature curves obtained from CUFSM for cross-sections A, B and C for single channels

3 Material properties

All specimens were manufactured using a conventional press-braking process. A series of tensile coupons were tested in order to determine the material properties of the test specimens. For each type of lipped channel used to construct the back-to-back specimens, one flat coupon was extracted from the center line of the web. Two corner coupons were also taken from the web-flange junctions in order to determine the effect of the cold-working process on the material properties. All coupons were taken from the end portions of test specimens after they were tested, since the beams were subject to strains in these regions which were low enough not to alter the material properties of the steel.

The flat coupons had a nominal gauge length of 57 mm and a width of 12.5 mm and each of them was instrumented with a 50 mm extensometer and two 5 mm strain gauges, one on each side of the coupon (Fig.4 (a)). The corner coupons had a nominal gauge length of 57 mm and a width of 6 mm and were tested in pairs to avoid introducing unwanted bending moments due to their asymmetric cross-sectional shape. Each pair of corner coupons was instrumented with a 50 mm extensometer and a 5 mm strain gauge attached to the outside of each coupon, as shown in Fig.4 (b).

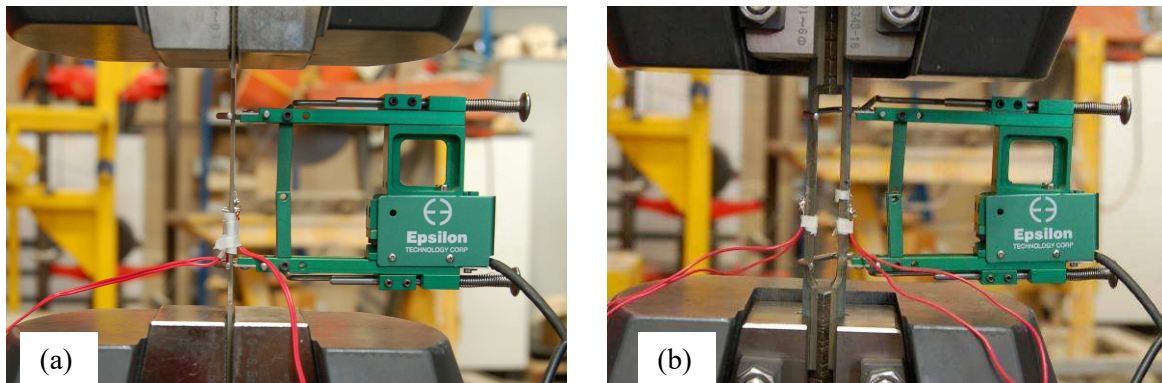


Fig.4 Tensile material tests for: (a) flat coupons (b) corner coupons

The coupons were tested in accordance with the specifications of the relevant European standard ISO E. 6892-1[33] . Table 4 lists the values of the material properties obtained for each flat coupon or set of corner coupons, where E is the Young's modulus, f_y is the 0.2% proof stress, σ_u is the ultimate tensile strength and ϵ_f is the elongation after fracture, measured over a gauge length of 50 mm. For the pair of corner coupons belonging to section B270, the elongation after fracture reported in Table 4 is lower than for the other corner coupons. This is due to the fact that the plastic deformations occurred slightly outside the gauge length, therefore this result should be disregarded.

Fig. 5 also presents the measured engineering stress-strain curves and the calculated true stress-strain curves of the tested flat coupons and pairs of corner coupons using the following equations:

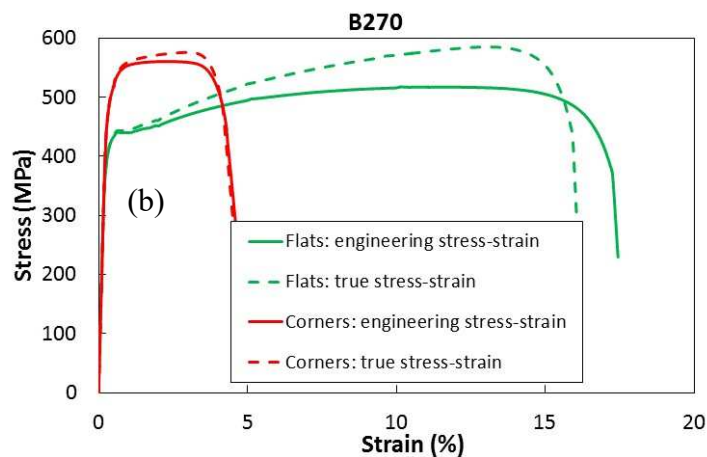
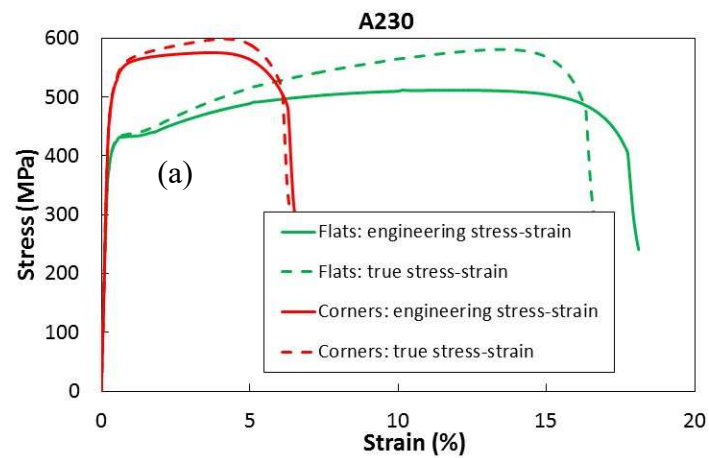
$$\sigma_{true} = \sigma(1 + \varepsilon) \quad (6)$$

$$\varepsilon_{true} = \ln(1 + \varepsilon) \quad (7)$$

where σ and ε are the measured engineering stress and strain, respectively, based on the original cross-section area of the coupon specimens. σ_{true} and ε_{true} are the calculated true stress and strain.

Table 4. Tensile properties of flat and corner coupons

Section	Types	E (GPa)	f_y (MPa)	σ_u (MPa)	ε_f (%)
A230	flat	196	416	511	18
	corner	218	516	575	6
B270	flat	199	424	517	17
	corner	208	508	560	(4)
C180	flat	200	427	521	18
	corner	209	514	576	7



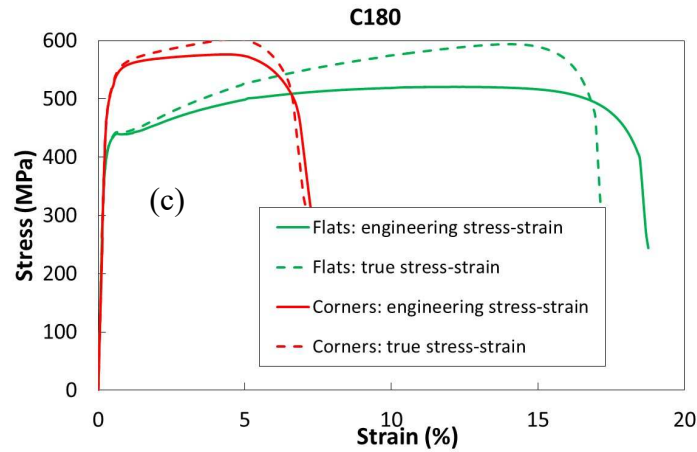


Fig.5 Stress–strain curves of the flat and corner coupons (tested as a pair)

4 Imperfection measurements

Geometric imperfections may significantly affect the stability of thin-walled CFS members, especially when coupled instabilities are involved [34]. For this reason, the magnitude and shape of the imperfections of each specimen were recorded before testing. As the beams were designed to fail through interaction of local and distortional buckling along the constant moment span (in between the loading points), only the out-of-plane imperfections along this region were of interest.

The test set-up shown in Fig.6 was used to measure these imperfections. A laser was mounted on an aluminium cross beam, which was moved in the longitudinal direction of the frame at a constant speed by an electric motor. A second electric motor allowed the laser to move in the perpendicular direction along the aluminium beam, thus enabling the laser to cover a rectangular area. The laser was able to measure the distance to the surface of the test specimens with an accuracy of 0.0075 mm . The laser moved along high precision bars with minimal tolerances and its ability to maintain a level measuring plane was verified against measurements of the nominally flat table underneath the frame in the absence of a test specimen. This flat table was guaranteed to be grade 3, providing a surface with a deviation from flatness of less than 0.06 mm [35]. During the measuring process, the translational speed of the laser was set to 5 mm/s , while the sampling rate was 5 Hz , resulting in one reading every millimetre.



Fig.6 Set-up used for imperfection measurements of single and back-to-back channel beams

The imperfections were measured along five lines in each cross-section, as shown in Fig.7. As an example, Fig.8 and Fig.9 show the measured imperfections of specimen A230-1 along lines ① to ⑤. The readings recorded along lines ①, ② and ③ provided information about the imperfections relevant for local buckling of the web, while the readings along lines ④ and ⑤ provided data on the imperfections affecting the distortional buckling mode. More specifically, the local imperfection was calculated by subtracting the average of lines ① and ③ from the readings taken along line ②. For the lipped channels, the distortional imperfection was taken as the maximum reading of lines ④ and ⑤.

It was recognized that assembling the channels in a back-to-back configuration might alter the imperfection profile and, therefore, the imperfections were measured before and after the assemblage of the built-up specimens. Before the specimens were assembled, the maximum amplitudes of the recorded local and distortional imperfections in the tested beams are provided in Table 5. The results indicate that the maximum out-of-plane imperfections encountered in the webs of the channels were of the order of 0.63 mm , while the lip-flange junctions of the lipped channels exhibited imperfections of up to 0.74 mm

After assembling the specimens, the maximum imperfections were 0.78 mm and 0.71 mm in both the webs and the flanges of the channels, as shown in Table 6. It is shown that the maximum local imperfections are not changed significantly due to the installation process. However, by comparing Fig.8 and Fig.9, it can be seen that the imperfection profiles themselves have changed as a result of the assembling process of the beams using torque wrench.

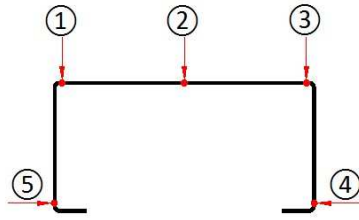


Fig.7 Locations of the imperfection measurements

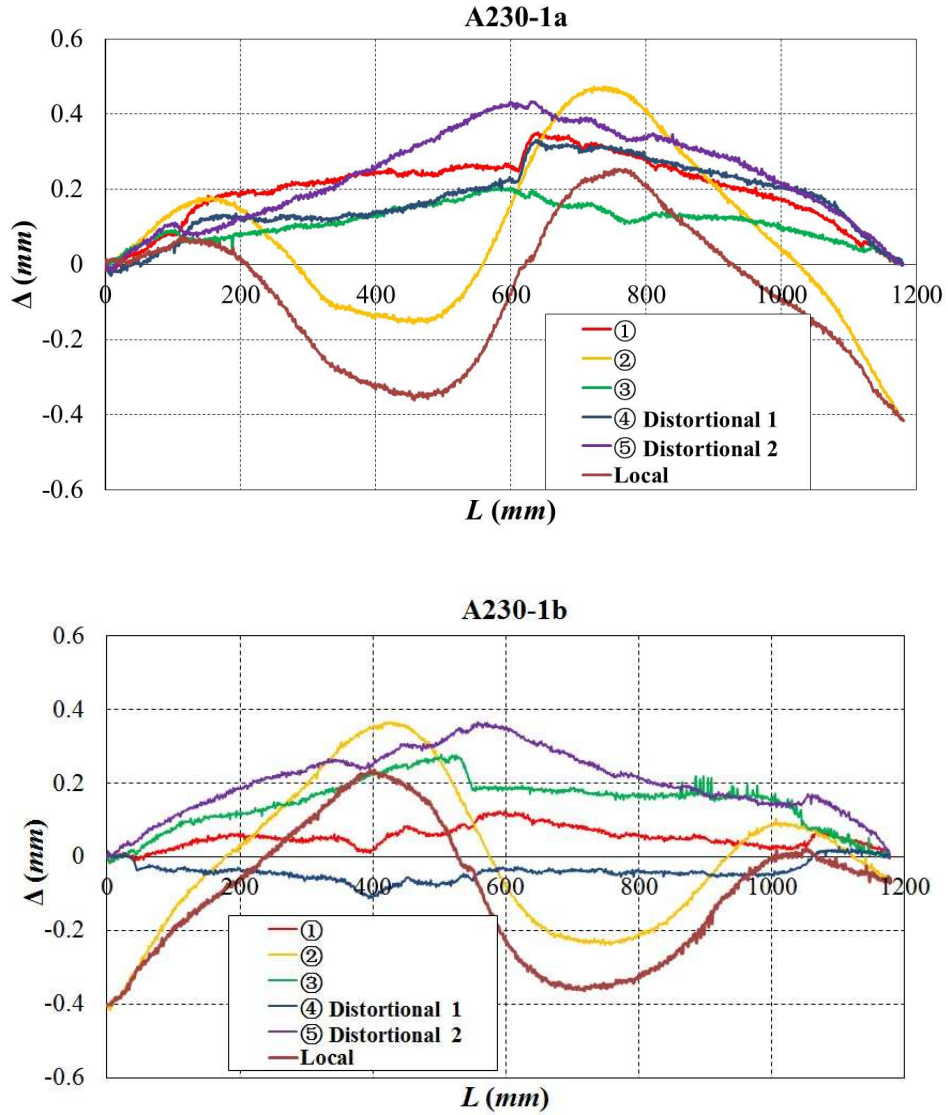


Fig.8 Typical imperfection distributions of channels before assembling

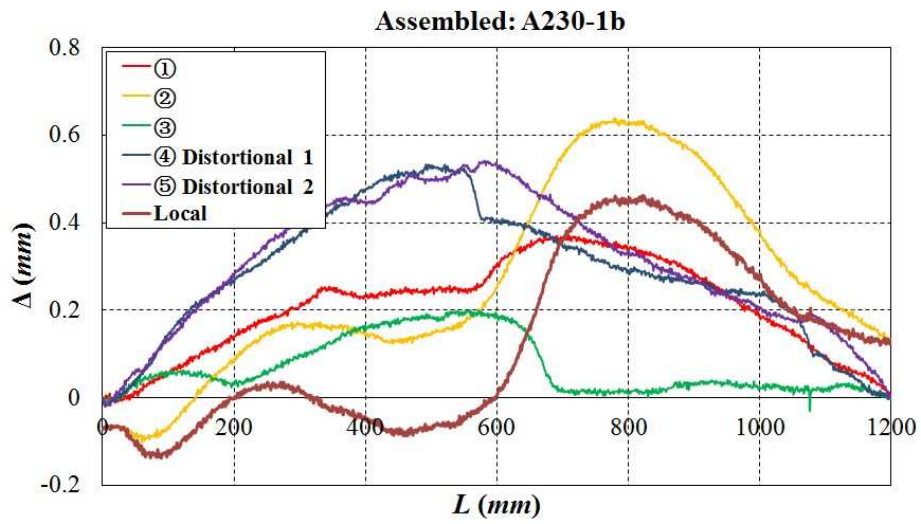
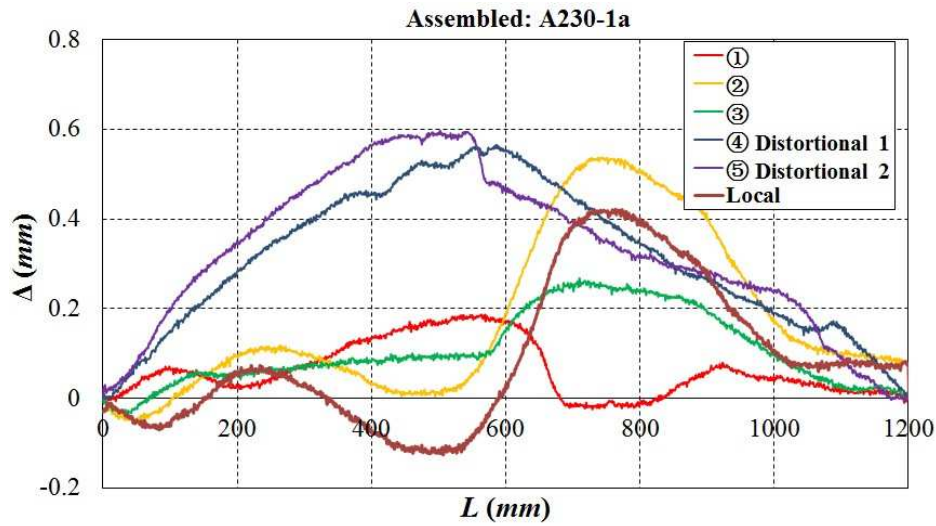


Fig.9 Typical imperfection distributions of channels after assembling

Table 5. Maximum amplitudes of local, distortional imperfections in single channel before assembling

Specimen	Local (mm)	Distortional (mm)
A230-1a	0.42	0.44
A230-1b	0.40	0.37
A230-2a	0.46	0.36
A230-2b	0.37	0.32
B270-1a	0.46	0.34
B270-1b	0.53	0.74
B270-2a	0.63	0.37
B270-2b	0.62	0.30
C180-1a	0.28	0.27
C180-1b	0.26	0.52
C180-2a	0.30	0.40
C180-2b	0.32	0.50

Table 6. Maximum amplitudes of local, distortional imperfections in single channel after assembling

Specimen	Local (<i>mm</i>)	Distortional (<i>mm</i>)
A230-1a	0.42	0.60
A230-1b	0.46	0.54
A230-2a	0.40	0.49
A230-2b	0.30	0.48
B270-1a	0.32	0.36
B270-1b	0.57	0.39
B270-2a	0.38	0.71
B270-2b	0.40	0.42
C180-1a	0.30	0.53
C180-1b	0.78	0.50
C180-2a	0.12	0.53
C180-2b	0.09	0.58

5 Test set-up

A total of six back-to-back beams were tested in a four-point bending configuration, as illustrated in Fig.10 (a). The specimens were supported on rollers located 3100 *mm* apart. All specimens were bent about their major axis. The loading system consisted of an actuator with a maximum capacity of 160 *kN* which imposed the load through a spreader beam onto the test specimens at two discrete locations 1200 *mm* apart. The spreader beam was restrained against out-of-plane movement by a specially designed guidance system, as shown in Fig.10 (b). Nylon blocks were used as bearing pads between the spreader beam and the uprights in order to reduce friction. A pin and a roller support were used to transfer the load from the spreader beam to the specimen. These supports were also designed to restrain any out-of-plane displacement of the top flange of the test specimen. Wooden blocks with a length of 250 *mm* were packed tightly into the cross-section at the loading points and end supports to avoid localized bearing failure, as shown in Fig.11. The shear force and bending moment diagrams of the tested beams are presented in Fig.12.

Three potentiometers with a stroke of 25 *mm* were placed under the test specimen at mid-span and under the two loading points in order to record the vertical deflections of the beam. Dial gages were placed at the supports to measure possible displacement in the vertical direction.

A displacement control scheme with a rate of 1 *mm/min* was used for all test specimens. The tests were halted for 4 *minutes* slightly before the peak load was reached, in order to eliminate strain-rate dependent effects. The tests were then continued and were terminated when the load went below 20% of the peak load on the descending path.

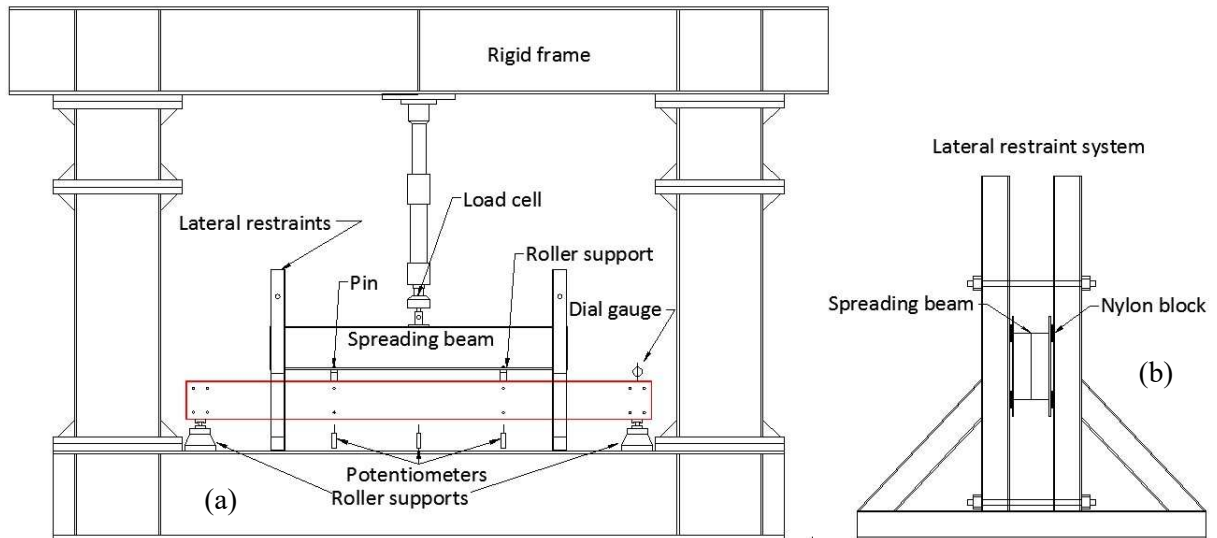


Fig.10 Schematic view of: (a) experimental set-up (b) lateral support system

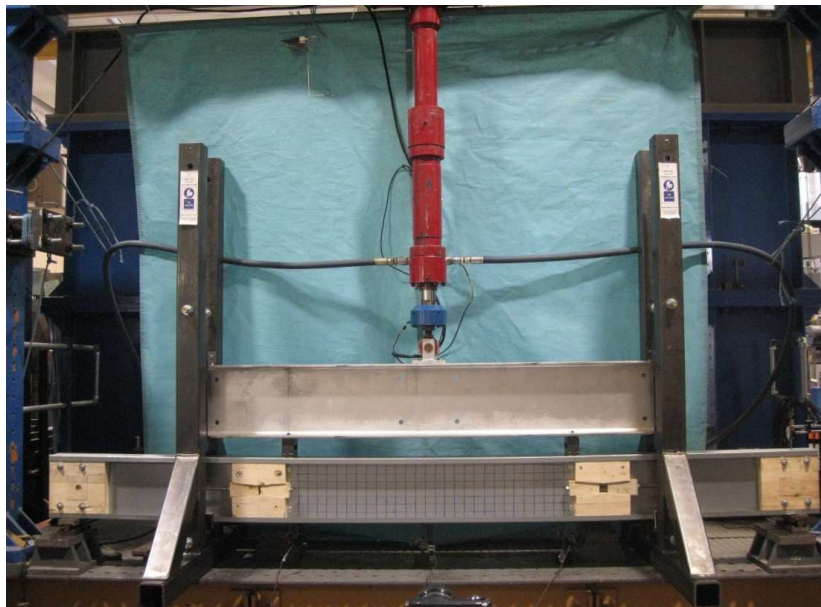


Fig.11 Four point-bending test set-up

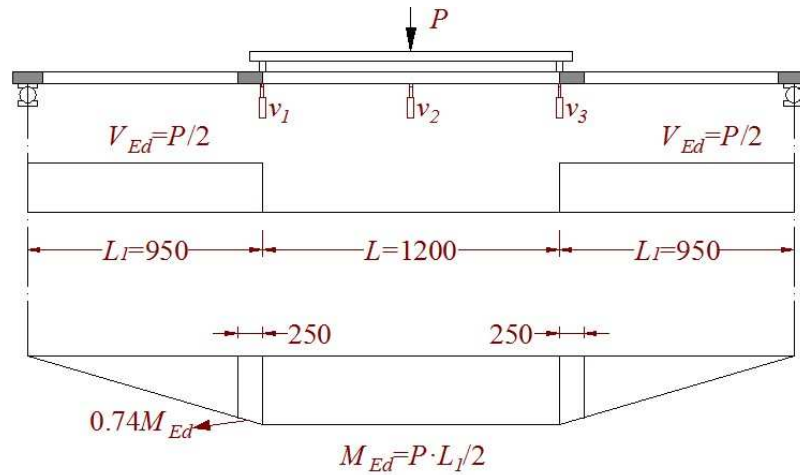


Fig.12 Bending moment and shear force diagrams of the tested beams

6 Test results

6.1 Deformed shape

As expected, all test specimens failed within the constant moment span by interaction of local and distortional buckling. In specimens C180 pure local buckling was first observed in the top flanges. This was due to the high slenderness of the flanges, which had a width-to-thickness ratio of 67, and the fact that they were subject to the highest compressive stress in the cross-section. As the bending moment increased, superimposed distortional buckling was recorded, as shown in Fig.13. Participation of the webs was also observed before the ultimate capacity of the specimens was reached.

Specimens A230 also failed due to interaction between local and distortional buckling, as shown in Fig.14. However, in these specimens the webs constituted the slenderest components of the cross-section, and therefore triggered local buckling in the web rather than the flange. As the load increased, the lips were unable to suppress the distortional mode.

Specimens B270 had the maximum web height, combined with relatively narrow flanges. Local buckling was again first detected in the webs of the channels, with distortional buckling participating at a higher load (Fig.15).

Past the peak load the buckling deformations localized in all specimens, forming an anti-symmetric yield line pattern in both flanges of the back-to-back channels.

All test specimens showed an anti-symmetric distortional buckled shape in which the top flange of one channel moved upward while the top flange of the other channel moved downward. It is to be noted that the webs of the channels were not connected by intermediate fasteners within the constant

moment span, and therefore the observed shape was a result of contact between the channel webs alone.

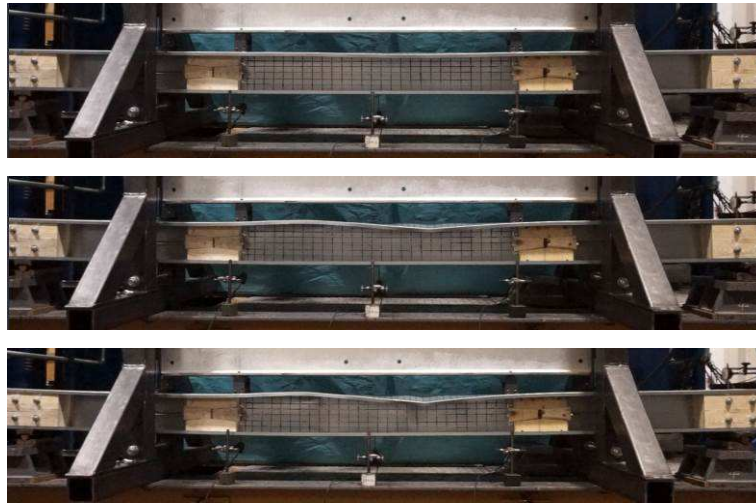


Fig.13 Failure progression in beam C180-2

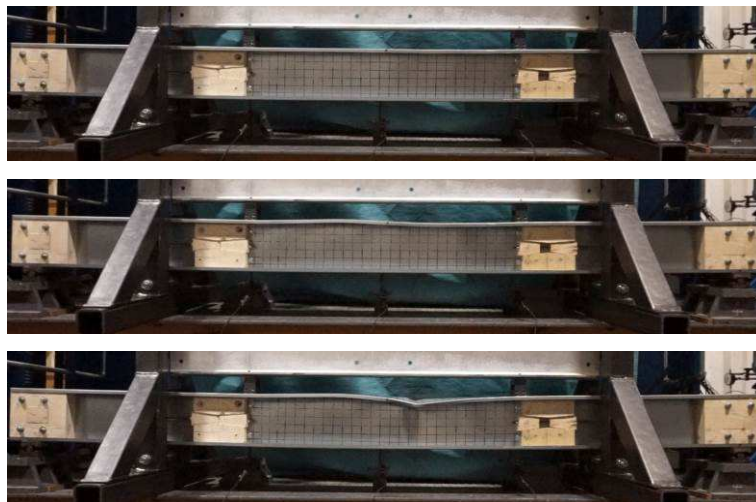


Fig.14 Failure progression in beam A230-2





Fig.15 Failure progression in beam C270-2

6.2 Moment-deformation curves

Fig.16 plots the bending moments against the mid-span deflections for all test specimens, where the moments were calculated from the measured concentrated load using the equations shown in Fig.12. The ultimate capacities of all test specimens are also listed in Table 12. In general, a good agreement was obtained within each set of twin specimens, with the ultimate capacities varying by less than 2% from each other. An exception to this occurred in specimens B270, where the ultimate capacity of specimen B270-1 was considerably lower than that obtained for its counterpart. This was due to the fact that specimen B270-1 was tested without wooden blocks under the load application points. As a result, web crippling occurred under the loading points in combination with local buckling which extended all along the constant moment span. Therefore, the results of test B270-1 should be disregarded.

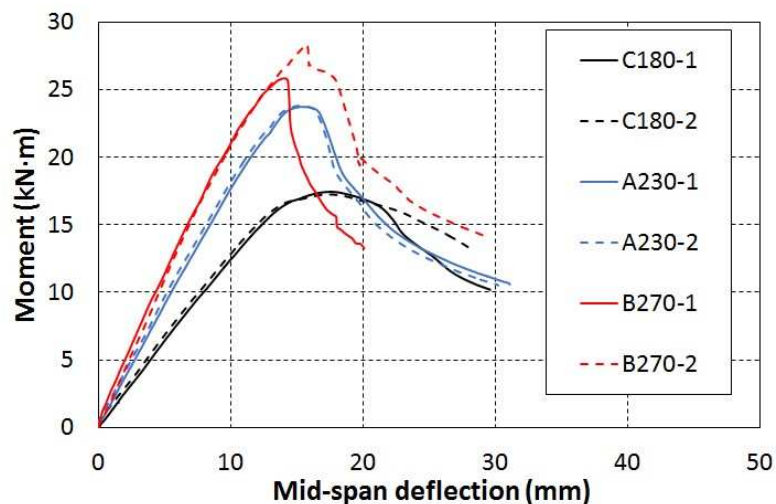


Fig.16 Moment vs mid-span deflection for all beams

The moment-curvature graphs obtained from the tests are shown in Fig.17, where the moment M was calculated using equations in Fig.12 and the curvature κ was calculated using the following formula [36]:

$$\kappa = \frac{2y}{y^2 + \left(\frac{L}{2}\right)^2} \quad (8)$$

where L is the mid span defined in Fig.17, y is a function of the vertical displacements measured at the 3 potentiometers, as shown in Fig.17. y is determined by assuming that the deflections form a part of a circular arc along the middle span:

$$y = v_2 - \frac{v_1 + v_3}{2} \quad (9)$$

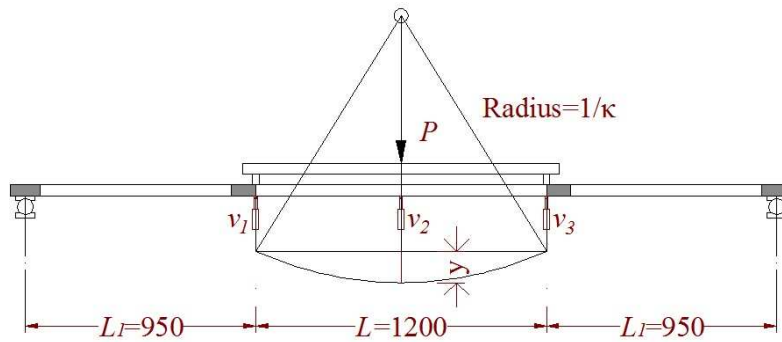


Fig. 17 Calculation of curvature using the displacement measured in potentiometers

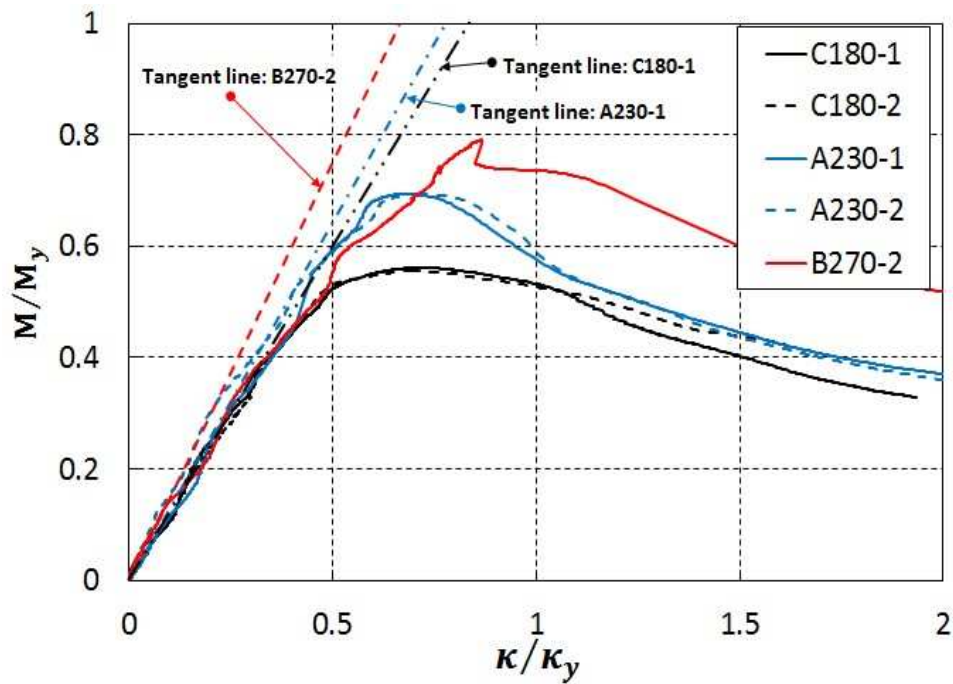


Fig.18 Non-dimensional moment-curvature curves for the tested beams

In Fig.18, the moment and curvature are non-dimensionlized with regard to the first yield bending moment $M_y = W_e f_y$ and the curvature κ_y which the first yield bending moment would produce if the beam behaved in a linear elastic way:

$$\kappa_y = \frac{M_y}{E \cdot I_y} \quad (10)$$

where W_e is the gross section modulus, E and f_y are the measured elastic modulus and the 0.2% proof stress. I_y is the moment of inertia of the back-to-back sections.

Fig.18 also plots 3 tangent lines from the initial elastic modulus of the curves. The moment-curvature curves of the tested beams for C180, A230 and B270 show a significant deviation from the linear range (stiffness reduction) at approximate bending moments of $0.4M_y$, $0.3M_y$ and $0.2M_y$, respectively, which indicates a reduced cross-sectional property at bending. After a nonlinear deformation phase, the bending moment reaches its peak value at the ultimate bending moment. The reduction in the bending moment at the ultimate moment was initiated by the local/distortional buckling of the top flanges in the pure bending span. It is also shown in Fig.18 that the ultimate bending moments are around 0.55, 0.70 and 0.79 times the bending moments at first yield for cross-sectional series of C180, A230 and B270, respectively, which indicates that the sections were failed before the material yielded.

7 Design rules for CFS beams

The design of CFS beams requires that consideration should be given to the Ultimate Limit State i.e. the strength of the member and the Serviceability Limit State: deflections likely to be not exceeded at service loads. As a result of the essentially thin-walled cross-sectional properties of the tested CFS members, the reduced stiffness due to the local/distortional buckling should be taken into account in the calculation of deflections of the tested beams. For the serviceability limit state design, it is anticipated that non-conservative results will be obtained when linear elastic properties are used rather than effective cross-sections.

7.1 Strength

The design of beams involves the determination of the bending strengths for local/distortional and global buckling, the shear strengths and the strength for combined bending and shear, as stipulated in Sections 6.1.4, 6.1.5, 6.1.10 of Eurocode 3 design guidelines.

Strength for bending only

The design bending capacity of a beam around its major axis can be calculated according to Clause 6.1.4.1 in Eurocode 3, Part 1-3 on the basis of the “effective width” method”:

$$M_{c,Rd1} = W_{eff} \cdot f_y \quad (11)$$

Due to the geometrically flexible cross-sectional shapes and nonlinear stress-strain hardening of CFS material properties, the inelastic strain may be used in CFS cross-sections subjected to bending. Yener and Pekoz [37, 38] proposed a design method that incorporates partial section plastification in the prediction of inelastic bending strength of CFS beams. The importance of this work lies in the fact that a relationship between the ultimate compressive edge strain and the slenderness ratios of the compressive flanges and webs has been determined, where the stress and strain distribution in a cross-section can be determined. The calculation of the ultimate capacity of CFS beams to take into account the inelastic reserve capacity is therefore straightforward. Later, Shifferaw and Schafer [39] studied the relationship between inelastic strain developed in cross-sections and the cross-section slenderness using detailed nonlinear Finite Element analysis and previous experimental results. Their work differs from that of Yener and Pekoz [37, 38] in the way that individual design formulations are developed to predict the inelastic local, distortional, and lateral-torsional buckling and to provide the Direct Strength Design formulations. Hui et al [40] recently investigated the moment redistribution of indeterminate CFS beams using the nonlinear Finite Element Method. Design formulas were proposed to predict the ultimate capacity of continuous beams considering stress redistribution. The research has improved the understanding of the mechanism of inelastic reserve in indeterminate CFS systems rather than cross-sections.

Eurocode 3, Part 1-3 allows the development and utilisation of the inelastic reserve capacity for the design of CFS beams subjected to bending. This has been taken into account in the evaluation of the objective functions presented in Eq.(1) during the optimization process. According to Eurocode 3, Part 1-3, there are two mechanisms on the development of inelastic reserve capacity in cold-formed steel members subjected to bending. The first mechanism is that first yield happens at the compressive flange. This constantly occurs when the cross-section bends around its major and symmetrical axis, as shown in Fig.19, where reduced widths of the compressive parts lead the neutral axis to shift to a lower position.

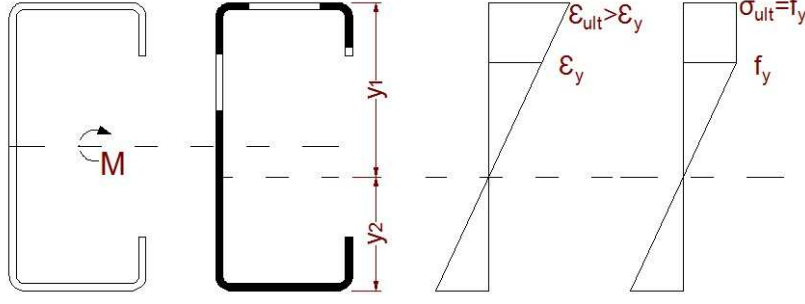


Fig.19 Inelastic bending stress and strain distribution of a lipped channel section

The bending strength can be calculated by using a function composed of three segments corresponding to the maximum slenderness of a decisive plate element in the cross-section, as shown in Fig.20. When the effective section modulus W_{eff} is equal to the gross section modulus W_e and the inelastic reserve capacity is allowed, the strength should be checked with the following equation:

$$\frac{M_{c,Rd1} - M_y}{M_p - M_y} = 4 \left(1 - \frac{\lambda_{e\max}}{\lambda_{e0}} \right) \quad (12)$$

where $M_y = W_e \cdot f_y$ is the classic moment at first yield of gross section, which has also been defined in Section 6.2. $M_p = W_p \cdot f_y$ is the fully plastic moment of gross section. $\lambda_{e\max}$ is the slenderness of the decisive element that has the largest value of λ_e / λ_{e0} . The slenderness λ_e and λ_{e0} for internal plate elements can be defined as:

$$\lambda_e = \lambda_p = \sqrt{\frac{f_y}{\sigma_{cr}}} \quad (13)$$

$$\lambda_{e0} = 0.5 + \sqrt{0.25 - 0.055(3 + \psi)}$$

where σ_{cr} is the elastic buckling stress of the plate element and ψ is the stress ratio. For outstand elements $\lambda_{e0} = 0.673$. The equation can be rearranged as:

$$M_{c,Rd1} = 4f_y \left[W_e + (W_p - W_e) \left(1 - \frac{\lambda_{e\max}}{\lambda_{e0}} \right) \right] \quad (14)$$

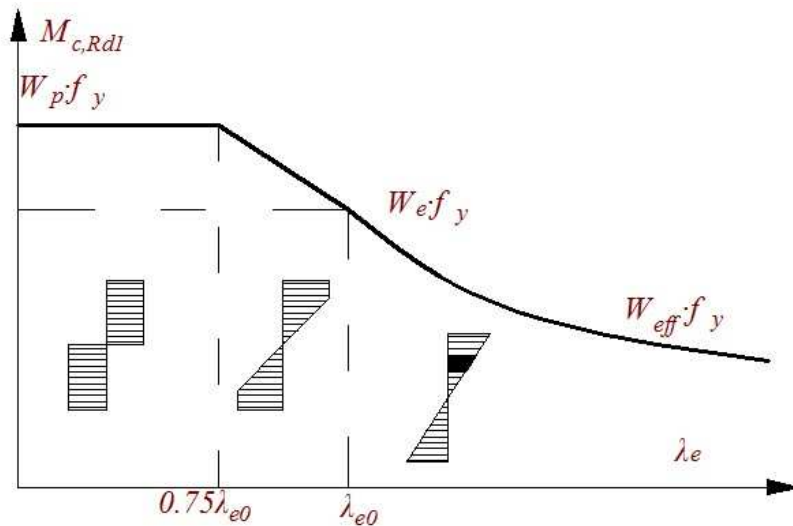


Fig.20 Bending strengths as a segmented function of slenderness of decisive elements

The other mechanism of inelastic reserve capacity is that first yield happens at the tension flange. This is the case when the cross-sectional shape of bending members is nonsymmetrical, and the local/distortional buckling in the compressive part reduces the effective widths of the plate elements. As shown in Fig.21, when a hat shape cross-section and a lipped channel bends around its minor axis, this leads the neutral axis to shift to a higher position. First yield therefore takes place at the tension flanges and Eurocode 3, Part 1-3 allows the usage of the inelastic reserve in Section 6.1.4.2. However, this will not happen in the tested lipped channels presented in this paper since all of the channels were bending around their major and symmetrical axis, which leads to a higher compressive stress at the top flange.

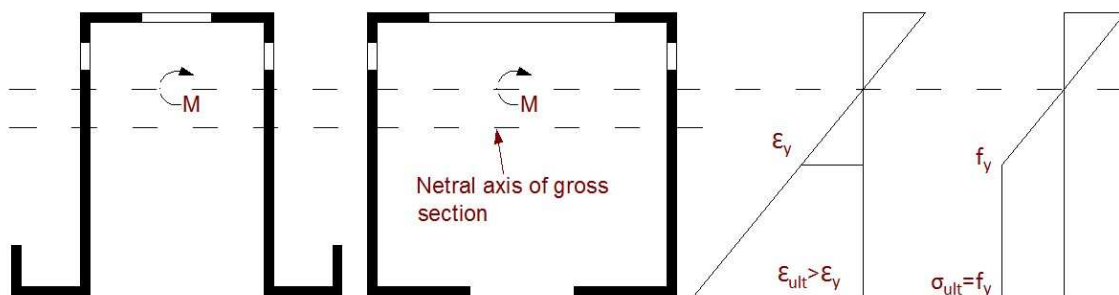


Fig.21 Inelastic bending stress and strain distribution of a hat section and a lipped channel bending around their minor axis

It is therefore concluded that the inelastic reserve capacity should be checked based on the Fig.19 and Fig.20 if effective section modulus W_{eff} is equal to the gross section modulus W_e . Table 7

presents the intermediate results of the cross-sectional properties and the resulting cross-sectional capacity of the tested specimens. It is worth noting that the cross-sectional dimensions, yield stress and elastic modulus used for the calculation of the strengths of all sections were from the tested results.

Table 7. Elastic and effective cross-sectional properties and bending capacity of the tested specimens

Specimens	I_{eff} (mm^4)	W_{eff} (mm^3)	I_y (mm^4)	W_e (mm^3)	$M_{c,Rd1}$ ($kN\cdot m$)
C180-1	4851804	44248	6536363	54417	18.89
C180-2	4964162	44582	6537890	55157	19.04
A230-1	7402600	53974	9461445	81839	23.05
A230-2	7460800	54562	9483281	82463	23.30
B270-1	9900200	64028	11664387	101429	27.34
B270-2	9867800	63608	11613466	100986	27.16

Lateral-torsional buckling

Eurocode 3, Part 1-3 uses a reduction factor χ_{LT} on the cross-sectional bending capacity to account for the lateral-torsional buckling. The reduction factor can be calculated using a global slenderness ratio $\lambda_{LT} = \sqrt{W_{eff} f_y / M_{cr}}$. The design bending strength $M_{c,Rd2}$ of a laterally unbraced beam is obtained from:

$$M_{c,Rd2} = \chi_{LT} \cdot W_{eff} \cdot f_y \quad (15)$$

$$\text{with } \chi_{LT} = \frac{1}{\Phi_{LT} + \sqrt{\Phi_{LT}^2 - \lambda_{LT}^2}} \leq 1.0 \quad (16)$$

$$\text{and } \Phi_{LT} = 0.5 \left[1 + 0.21 (\bar{\lambda}_{LT} - 0.2) + \lambda_{LT}^2 \right] \quad (17)$$

Considering a channel beam subjected to equal end moments about the major axis, as in the pure bending span in the tests, the elastic lateral-torsional buckling load M_{cr} can be calculated in terms of the unbraced length and the section properties of the gross section as follows:

$$M_{cr} = \frac{\pi}{L} \sqrt{EI_z \left(GJ + \frac{\pi^2 EI_w}{L^2} \right)} \quad (18)$$

where EI_z is the flexural rigidity about the minor axis, EI_w is the warping rigidity, GJ is the torsional rigidity and $L=1200 \text{ mm}$ indicates the unbraced length in the tests. In calculation of the cross-sectional properties of the tested beams in Table 8, an I-shaped section with a double thickness in the web is used as equivalent to original the back-to-back section, as shown in Fig.22. It can be

seen in Table 8 that the reduction factor is slightly smaller than 1.0, leading to a small reduction in bending capacity compared to the cross-sectional capacities presented in Table 7. It is worth noting that lateral-torsional buckling didn't occur in the tested specimens. It can also be seen from Table 8 that with the same amount of material, the reduction factor of specimens with deeper cross-section is smaller, leading to more reduction in critical buckling moment. However, the optimum cross-sections (B270 series) still have higher bending capacities, even with slightly smaller reduction factors for lateral-torsional buckling.

Table 8. Design strengths of the tested beams to lateral-torsional buckling

Specimens	I_w ($\times 10^{10}$ mm^6)	J (mm^4)	I_z (mm^4)	W_{eff} (mm^3)	M_{cr} ($kN\cdot m$)	χ_{LT}	$M_{c,Rd2}$ ($kN\cdot m$)
C180-1	2.3080	2216	2938982	44248	358.0	0.9934	18.77
C180-2	2.3111	2201	2941008	44582	358.3	0.9933	18.91
A230-1	1.7771	2551	1360923	53974	209.8	0.9711	22.38
A230-2	1.7249	2566	1333899	54562	204.6	0.9696	22.59
B270-1	1.0707	2869	576232	64028	107.9	0.9238	25.26
B270-2	1.0613	2802	573384	63608	107.2	0.9238	25.09

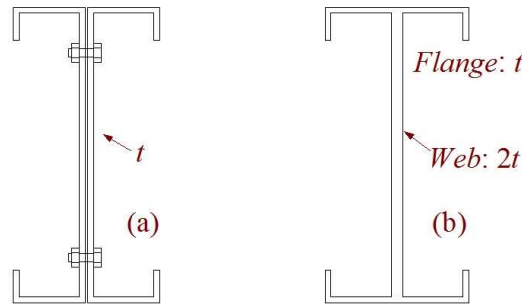


Fig.22 Cross-section to calculate the critical lateral torsional buckling: (a) Back-to-back section and (b) Equivalent I section

Strength for shear only

According to Section 6.1.5 of Eurocode 3, Part 1-3, the nominal shear strength $V_{b,Rd}$ of a CFS lipped channel beam should be obtained from the following equation:

$$V_{b,Rd} = h_w \cdot t \cdot f_{bv} \quad (19)$$

where h_w is the web height between the middle lines of the flanges in the lipped channel beam, t is the thickness of the section and f_{bv} is the shear strength considering buckling. According to the

stiffening condition of the webs at supports, f_{bv} can be calculated using the formulations shown in Table 9 according to the web slenderness defined as following:

$$\bar{\lambda}_w = 0.346 \frac{h_w}{t} \sqrt{\frac{f_y}{E}} \quad (20)$$

Table 9. Shear buckling strength f_{bv}

Relative web slenderness $\bar{\lambda}_w$	Web without stiffening at support	Web with stiffening at support
$\bar{\lambda}_w \leq 0.83$	$0.58f_y$	$0.58f_y$
$0.83 < \bar{\lambda}_w < 1.4$	$0.48 f_y / \bar{\lambda}_w$	$0.48 f_y / \bar{\lambda}_w$
$\bar{\lambda}_w \geq 1.4$	$0.67 f_y / \bar{\lambda}_w^2$	$0.48 f_y / \bar{\lambda}_w$

It is worth noting that wood blocks were used in conjunction with a restraining frame to prevent the distortion of the webs and to resist possible excessive local reactions at the supports in the tested beams. The case with web stiffening at supports is therefore taken into account to verify the design. For each back-to-back section, the cross-sectional properties of the individual channel is calculated to obtain the shear capacities and then the shear capacities are added together to obtain the full strength of the back-to-back specimen. The intermediate results are shown in Table 10, it can be seen that the ratio of applied maximum shear force to the shear buckling strength is in the range of 0.31-0.51, which is far less than the failure capacity. The original test set-up is therefore able to prevent the possible shear buckling failure.

Table 10. Shear strengths of the tested beams

Specimens	$\bar{\lambda}_w$	f_{bv} (MPa)	$V_{b,Rd1}$ (kN)	$V_{b,Rd}$ (kN)	V_{Ed} (kN)	$V_{Ed}/V_{b,Rd}$
C180-1a	1.9039	107.7	29.41	59.33	18.36	0.31
C180-1b	1.8866	108.6	29.92	59.33	18.36	0.31
C180-2a	1.9000	107.9	29.63	59.05	18.17	0.31
C180-2b	1.9051	107.6	29.42	59.05	18.17	0.31
A230-1a	2.4118	82.8	29.12	57.80	24.97	0.43
A230-1b	2.4301	82.2	28.68	57.80	24.97	0.43
A230-2a	2.4222	82.4	28.81	57.93	25.05	0.43
A230-2b	2.4107	82.8	29.12	57.93	25.05	0.43
B270-1a	2.8297	71.9	29.51	59.14	27.72	0.47
B270-1b	2.8338	71.8	29.63	59.14	27.72	0.47
B270-2a	2.8509	71.4	29.21	58.17	29.83	0.51
B270-2b	2.8692	70.9	28.96	58.17	29.83	0.51

Strength for combined bending and shear

Prior to the tests, the members were designed to prevent the failure of the side spans through combined bending and shear. Eurocode 3, Part 1-3 stipulates that cross-sections should be designed subjected to combined action of bending moment M_{Ed} and shear force V_{Ed} :

$$r_{MV} = \frac{M_{Ed}}{M_{c,Rd}} + \left(1 - \frac{M_{f,Rd}}{M_{pl,Rd}}\right) \left(\frac{2V_{Ed}}{V_{b,Rd}} - 1\right)^2 \leq 1.0 \quad (21)$$

where r_{MV} is the ration of the resistance, $M_{f,Rd}$ is the moment resistance of a cross-section consisting of the effective widths of top and bottom flanges, $M_{pl,Rd}$ is the plastic moment of resistance of the cross-section which consists of the effective widths of flanges and the fully effective width of the webs, as shown in Fig.23. The contribution of the flanges to the shear buckling resistance has been taken into account in the interactive design formulation.

Table 11 lists the calculated ratio of the design equation presented in Eq.(21). Due to the wood blocks inserted at the loading position, the cross-section is taken at 250 mm away from the loaded points, as shown in Fig.12, and the cross-section is verified using the corresponding bending moment and shear force. It is shown in Table 11 that the ratios of the interaction equation are less than 1.0, which indicates that the interaction of shear buckling and bending is not the critical failure mode. This has been validated in the test that no failure modes of combined shear buckling and bending were observed.

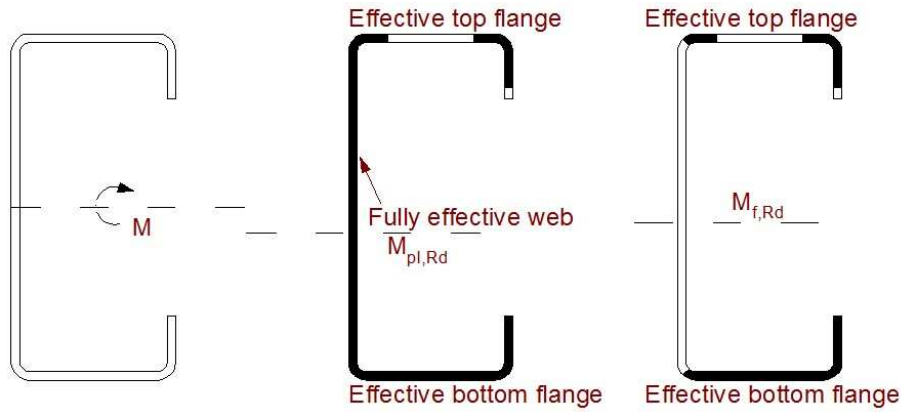


Fig.23 Cross-sections for the calculation of $M_{pl,Rd}$ and $M_{f,Rd}$

Table 11. Interaction of bending and shear on the design of the tested beams

Specimens	$V_{b,Rd}$ (kN)	$M_{c,Rd}$ (kN·m)	$M_{f,Rd}$ (kN·m)	$M_{pl,Rd}$ (kN·m)	r_{MV}
C180-1	59.33	18.89	17.73	28.69	0.74
C180-2	59.05	19.04	17.85	28.87	0.73
A230-1	57.80	23.05	19.17	35.91	0.77
A230-2	57.93	23.30	19.30	36.09	0.76
B270-1	59.14	27.34	21.17	44.04	0.71
B270-2	58.17	27.16	20.90	43.83	0.77

Comparison of proposed design strength with test

Table 12 also compares the ultimate capacities obtained from the experiments with the predictions given by Eurocode 3, using the equations presented in Eq.(11) and Eq.(15), cross-sectional dimensions in Table 1-3 and the material properties in Table 4. When calculating the effective cross-sectional properties according to the Eurocode, full iterations were carried out (which are not strictly prescribed by the Eurocode)[27]. These iterations are necessary because the location of the neutral axis of the effective cross-section is initially unknown and also because of the interaction between the local and distortional buckling modes. The measured dimensions and the material properties obtained from the coupon tests were used. In general, Table 12 shows that a good agreement was achieved between the experimental and the calculated bending capacities ($M_{c,Rd2}$ in Eq.(15)) of the back-to-back lipped channel beams, with the ratio of the Eurocode predicted values to the test results ranging from 0.89 to 1.10, depending on the cross-section type. The average ratio is 0.99 with a standard deviation of 0.09. It is also shown in Table 12 that the cross-sectional bending capacity is generally well predicted with Eurocode 3. The ratio of the Eurocode predicted cross-sectional

bending capacity $M_{c,Rd1}$ to the test values ranges from 0.96-1.10, with an average ratio of 1.02 and a standard deviation of 0.07, which is slightly unconservative. Similar accuracies have been obtained by other [41]. Since the failure mode of lateral torsional buckling has not been observed, the reduction factor of lateral-torsional buckling leads to a slightly reduced bending capacity, providing a conservative prediction instead of a generally unconservative prediction of cross-sectional capacity.

Table 12. Ultimate capacities of the test specimens

Specimen	Test ($kN\cdot m$)	Eurocode 3		$M_{c,Rd1} / \text{Test}$	$M_{c,Rd2} / \text{Test}$
		$M_{c,Rd1}$ ($kN\cdot m$)	Eurocode 3 $M_{c,Rd2}$ ($kN\cdot m$)		
C180-1	17.43	18.89	18.77	1.08	1.08
C180-2	17.24	19.04	18.91	1.10	1.10
A230-1	23.72	23.05	22.38	0.97	0.94
A230-2	23.79	23.3	22.59	0.98	0.95
B270-1	(25.83)	27.34	25.26	--	--
B270-2	28.34	27.16	25.09	0.96	0.89
Average				1.02	0.99
St. Dev.				0.07	0.09

7.2 Deflections

According to Eurocode 3, Part 1-3, the effective cross-sectional properties should be used in all the serviceability limit state calculations for CFS member design. In determination of the cross-sectional properties with the distribution of bending moments, the effective parts of individual plates in the cross-section will be different according to the stress distribution. The effective moment of inertia can be taken as variable along the span according to the stress level at specific locations. However, a uniform value can be specified conservatively, based on the absolute maximum moment under serviceability loading.

Eurocode 3, Part 1-3 calculates the effective moment of inertia $I_{fic}(x)$ by using an interpolation between the gross cross-sectional properties I_y and the effective cross-section properties $I(\sigma_{com})$ calculated at a maximum stress level σ_{com} within the span length:

$$I_{fic}(x) = I_y - \frac{\sigma_y(x)}{\sigma_{com}} (I_y - I(\sigma_{com})_{eff}) \quad (22)$$

The calculation process is therefore as shown below, using the constant modulus of elasticity (E) at the initial stage of the nonlinear stress-strain curve:

$$P \rightarrow M(x) \rightarrow \sigma_y(x) \rightarrow b_{eff} \rightarrow I_{eff} \rightarrow I_{fic}(x) \rightarrow d = \int_0^{L_2} \frac{M(x) \cdot x}{E \cdot I_{fic}(x)} dx \quad (23)$$

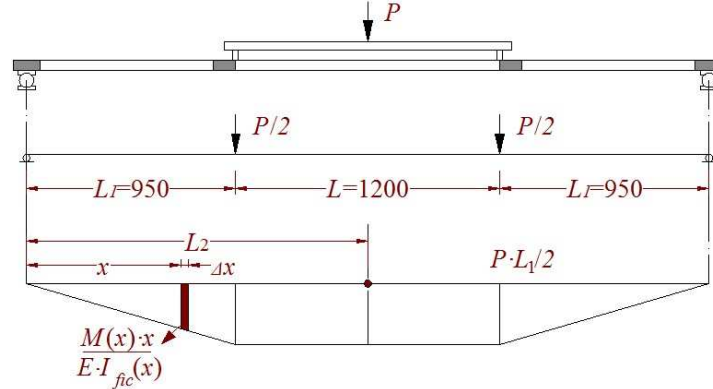
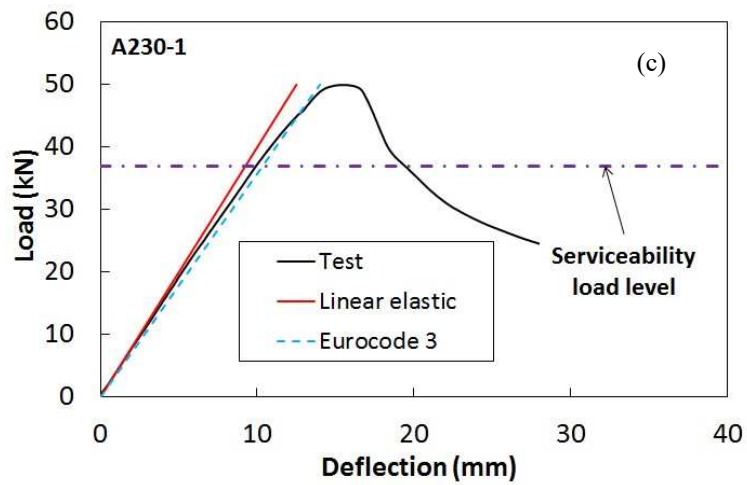
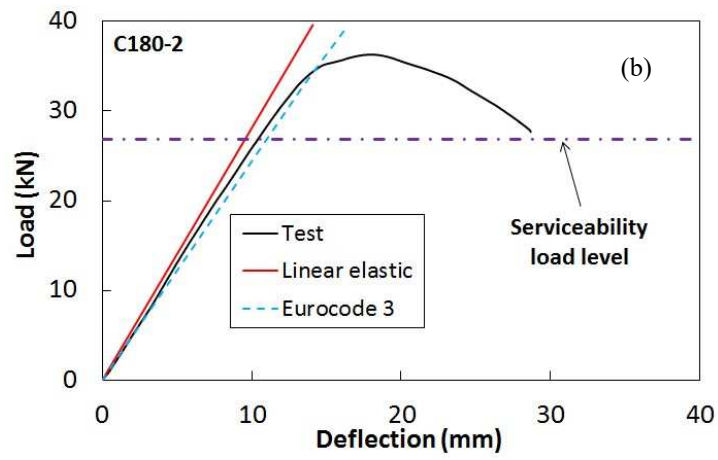
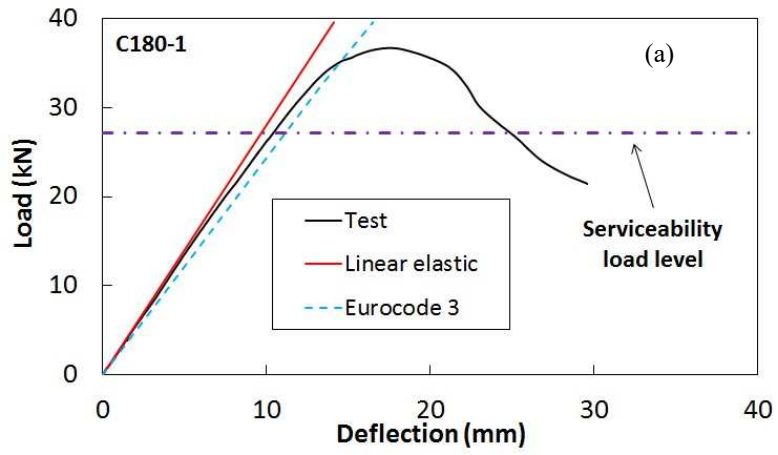


Fig.24 Calculation of the deflection in the mid span

A trapezoidal rule is used for the integration of the function to calculate the deflections at mid span. The domain of integral $[0, L_2]$ is firstly divided into n equal lengths with each subinterval in length of $\Delta x = x_k - x_{k-1}$. The deflection is therefore calculated as:

$$d = \int_0^{L_2} \frac{M(x) \cdot x}{E \cdot I_{fic}(x)} dx = \sum_{k=1}^n \frac{M(x_{k-1}) \cdot x_{k-1} / E \cdot I_{fic}(x_{k-1}) + M(x_k) \cdot x_k / E \cdot I_{fic}(x_k)}{2} \Delta x \quad (24)$$

Fig.25(a)-(e) plots the load deflection curves at the mid span of the tested specimens. The deflections, calculated by using the reduced stiffness presented in Eurocode 3 as per Eqs.(22)-(24) are presented in the figures using a dashed line and compared with the tested curves, as shown in Fig.25. Fig.25 also includes the load-deflections produced by using the linear elastic properties of the tested cross-sections. By comparing the results presented over a wide range of load levels, it is shown that the linear elastic method generally provides an underestimation while the Eurocode 3 method is slightly conservative, below a load level of approximately 0.9 times of the ultimate capacity. After this load level, the Eurocode 3 method underestimates the deflection.



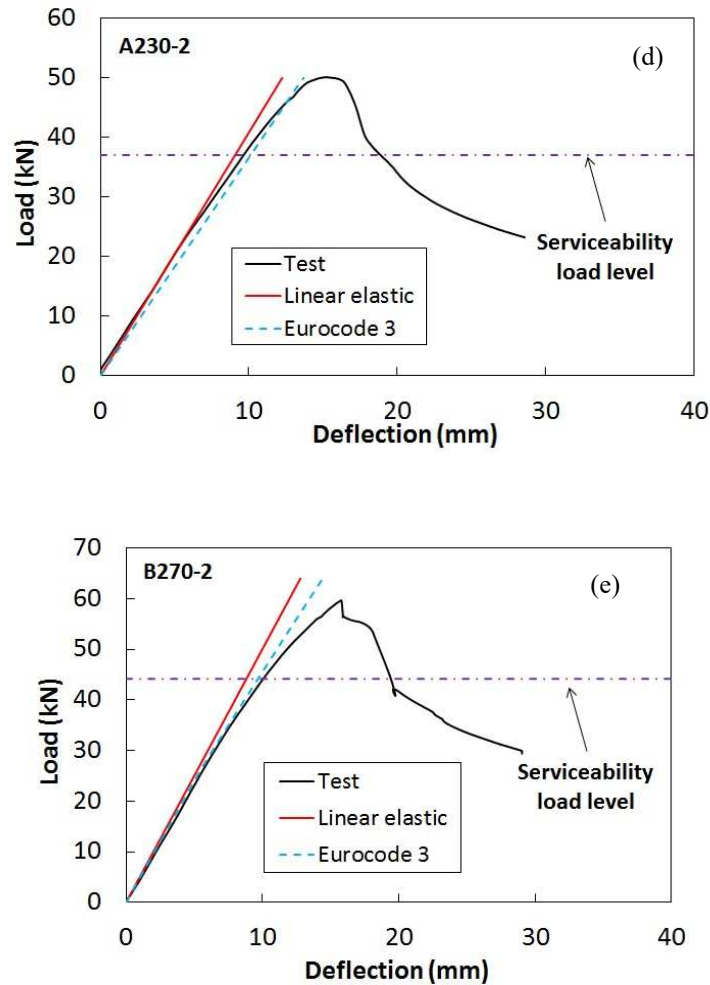


Fig.25 Load deflection curves for the tested specimens at mid span in four point bending tests

However, the deflections are limited by using the serviceability load levels, as illustrated in Section 2. Table 13 therefore presents the deflections calculated at the load level of 0.74 times ultimate capacity, using both the linear elastic and the effective cross-sectional properties. The use of linear elastic properties of the cross-sections (full section properties) leads to underestimated deflections compared to the experimental results, the amount of the underestimation of deflection being 4% on average, with a standard deviation of 7%. When using the reduced cross-sectional properties to calculate the deflections, Eurocode 3 overestimates the deflections by 6% on average, with a standard deviation of 3% at the serviceability load level. It is worth noting that the calculated deflections are less than the limit of $L/200$, as presented in Section 2.

Table 13. Comparison of the tested and calculated deflections using linear elastic property and Eurocode 3 at serviceability load level.

Specimens	d_{test} (mm)	$d_{elastic}$ (mm)	$d_{Eurocode}$ (mm)	$\frac{d_{elastic}}{d_{test}}$	$\frac{d_{Eurocode}}{d_{test}}$
C180-1	10.4	9.7	11.1	0.93	1.07
C180-2	10.4	9.5	11.0	0.91	1.06
A230-1	9.9	9.2	10.3	0.93	1.04
A230-2	9.7	9.1	10.1	0.94	1.04
B270-2	8.9	9.7	9.9	1.09	1.11
Average				0.96	1.06
St. Dev.				0.07	0.03

8 Evaluation of the optimisation process

The tests also allowed an evaluation of the efficiency of the optimisation framework previously presented in [27, 28] and briefly summarized in Section 2. While section A is a standard commercially available cross-section and section C is an additional non-optimum solutions, section B is the lipped channel with the highest cross-sectional bending capacity subject to the design and manufacturing constraints presented in Eqs. (2)-(5). It is seen from Table 12 that the experiments confirm the optimisation results and demonstrate that the optimised lipped channel section (type B) offers a considerably higher bending capacity compared to the standard lipped channel section (type A) with the same amount of material. It is seen that the adopted optimisation method, even after considering design and manufacturing constraints, was able to increase the cross-sectional bending capacity by 17.8% and the capacity of the laterally unrestrained beam by 12.1%.

The serviceability requirement has been taken into account as a constraint in the optimisation framework. The effective cross-sectional properties have been used in the calculation of deflections in the standard and optimised beams. It was found that the serviceability constraints have been automatically satisfied within the optimisation process. This has been confirmed in the experimental study that the deflection of the optimised cross-section (Cross-section B) at the serviceability load level is 10% less than that of the standard cross-section (Cross-section A).

9 Conclusions

A total of six back-to-back beams, constructed from lipped channels with three different cross-sectional geometries were tested, to investigate the interaction between local and distortional buckling and to verify a previously proposed optimisation framework. The specimens were tested in a four-point bending configuration with simply supported boundary conditions, while being laterally

braced close to the supports. The geometric imperfections were recorded before and after the back-to-back specimens were assembled. Coupons extracted from the flat portions and the corner regions of each cross-section type were also tested to determine material properties. The ultimate capacities of the tested beams were predicted by using Eurocode 3 design method and deflections were calculated by the linear elastic method and the Eurocode 3 reduced stiffness method. The following conclusions can be obtained from this paper:

(1) All specimens failed due to interaction of local and distortional buckling, with local buckling being the primary buckling mode. In specimens C180, which displayed the widest flanges and the shallowest webs, local buckling originated in the top flanges, while in specimens A230 and B270, which have a deeper cross-section and a smaller flange width, local buckling was triggered in the web.

(2) A good agreement in the ultimate capacities was generally obtained within each set of twin beams, with the difference being less than 2 %. A comparison between the predictions given by Eurocode 3 and the experimental results indicated that Eurocode 3 is accurate in predicting the ultimate capacity of back-to-back lipped channel beams. The average ratio of the Eurocode predicted bending capacity to the experimental capacity was 0.99 with a standard deviation of 0.09.

(3) With the same amount of material, the adopted optimisation method, even after considering design and manufacturing constraints, was able to increase the cross-sectional capacity by 17.8% and the capacity of the laterally unrestrained beam by 12.1%.

(4) Eurocode 3 Part 1-3, which uses reduced cross-sectional properties to calculate deflections, can provide reasonable but slightly overestimated deflections at the serviceability load. However, using linear elastic full cross-sectional properties consistently underestimates the deflections.

(5) The previously proposed optimisation framework is effective in increasing the strength and stiffness of CFS elements in bending. The presented experimental and analytical study on the ultimate limit state and serviceability limit state of optimised and standard CFS elements in bending has also highlighted the importance of incorporating specific design requirements in the optimisation process of structural systems. The strengths in bending, shear, combined bending and shear and deflections of CFS back-to-back beams should be considered in future optimisations of frames using Eurocode 3.

Acknowledgments

This work was supported by EPSRC grant EP/L019116/1 and authors would like to thank the EPSRC for their financial support. The authors also would like to express their gratitude to BW Industries, UK, for providing the test specimens.

References

- [1] Fiorino L, Iuorio O, Landolfo R. Designing CFS structures: The new school bfs in naples. *Thin Wall Struct* 2014;78:37-47.
- [2] Lim JBP, Nethercot DA. Finite element idealization of a cold-formed steel portal frame. *Journal of Structural Engineering* 2004;130:78-94.
- [3] Lim JBP, Nethercot DA. Ultimate strength of bolted moment-connections between cold-formed steel members. *Thin Wall Struct* 2003;41:1019-39.
- [4] Wang HM, Zhang YC. Experimental and numerical investigation on cold-formed steel C-section flexural members. *J Constr Steel Res* 2009;65:1225-35.
- [5] Yu C, Schafer BW. Local buckling tests on cold-formed steel beams. *J Struct Eng-Asce* 2003;129:1596-606.
- [6] Yu C, Schafer BW. Distortional buckling tests on cold-formed steel beams. *J Struct Eng-Asce* 2006;132:515-28.
- [7] Hsu H-L, Chi P-S. Flexural performance of symmetrical cold-formed thin-walled members under monotonic and cyclic loading. *Thin Wall Struct* 2003;41:47-67.
- [8] Laim L, Rodrigues JPC, da Silva LS. Experimental and numerical analysis on the structural behaviour of cold-formed steel beams. *Thin Wall Struct* 2013;72:1-13.
- [9] Chen Y, Chen X, Wang C. Experimental and finite element analysis research on cold-formed steel lipped channel beams under web crippling. *Thin Wall Struct* 2015;87:41-52.
- [10] Manikandan P, Sukumar S, Balaji T. Effective Shaping of Cold-Formed Thin-Walled Built-up Beams in Pure Bending. *Arab J Sci Eng* 2014;39:6043-54.
- [11] Wang LP, Young B. Behavior of Cold-Formed Steel Built-Up Sections with Intermediate Stiffeners under Bending. I: Tests and Numerical Validation. *Journal of Structural Engineering* 2016;142.
- [12] Wang LP, Young B. Behavior of Cold-Formed Steel Built-Up Sections with Intermediate Stiffeners under Bending. II: Parametric Study and Design. *Journal of Structural Engineering* 2016;142.
- [13] Keerthan P, Mahendran M. Experimental studies on the shear behaviour and strength of LiteSteel beams. *Eng Struct* 2010;32:3235-47.
- [14] Von Karman T, Sechler EE, Donnell L. The strength of thin plates in compression. *Trans ASME* 1932;54:53-7.
- [15] AISI. North American specification for the design of cold-formed steel structural members, 2007 Edition. AISI S100-07. Washington, DC2007.
- [16] (ECS) ECFS. Eurocode 3: Design of steel structures-part 1.3, general rules-supplementary rules for cold-formed members and sheeting. Brussels2006.
- [17] Adeli H, Karim A. Neural network model for optimization of cold-formed steel beams. *J Struct Eng-Asce* 1997;123:1535-43.
- [18] Lee J, Kim SM, Park HS, Woo YH. Optimum design of cold-formed steel channel beams using micro Genetic Algorithm. *Eng Struct* 2005;27:17-24.
- [19] Lee JH, Kim SM, Park HS. Optimum design of cold-formed steel columns by using micro genetic algorithms. *Thin Wall Struct* 2006;44:952-60.
- [20] Tian Y, Lu T. Minimum weight of cold-formed steel sections under compression. *Thin-Walled Structures* 2004;42:515-32.
- [21] Schafer B. CUFSM Version 3.12. Department of Civil Engineering, Johns Hopkins University; 2006. p. <http://www.ce.jhu.edu/bschafer/cufsm/>.
- [22] Li Z, Schafer BW. Buckling analysis of cold-formed steel members with general boundary conditions using CUFSM: conventional and constrained finite strip methods. *Proceedings of the 20th Int2010*.
- [23] Leng JZ, Guest JK, Schafer BW. Shape optimization of cold-formed steel columns. *Thin Wall Struct* 2011;49:1492-503.
- [24] Leng J, Li Z, Guest JK, Schafer BW. Shape optimization of cold-formed steel columns with fabrication and geometric end-use constraints. *Thin Wall Struct* 2014;85:271-90.
- [25] Madeira J, Dias J, Silvestre N. Multiobjective optimization of cold-formed steel columns. *Thin Wall Struct* 2015;96:29-38.
- [26] Wang CA, Zhang ZN, Zhao DQ, Liu QQ. Compression tests and numerical analysis of web-stiffened channels with complex edge stiffeners. *J Constr Steel Res* 2016;116:29-39.
- [27] Ye J, Hajirasouliha I, Becque J, Eslami A. Optimum design of cold-formed steel beams using Particle Swarm Optimisation method. *J Constr Steel Res* 2016;122:80-93.
- [28] Ye J, Hajirasouliha I, Becque J, Pilakoutas K. Development of more efficient cold-formed steel channel sections in bending. *Thin Wall Struct* 2016;101:1-13.

- [29] CEN. Eurocode 3: Design of Steel Structures, part 1-5: Plated structural elements. Brussels: European Committee for Standardization; 2005.
- [30] CEN. Eurocode 3: design of steel structures, part 1.3: general rules—supplementary rules for cold formed members and sheeting. Brussels: European Committee for Standardization; 2005.
- [31] CEN. Eurocode 3: Design of Steel Structures. Part 1-1: General Rules and Rules for Buildings. Brussels: European Committee for Standardization; 2005.
- [32] Rhodes J. Design of cold formed steel members: Elsevier Applied Science; 1991.
- [33] ISO E. 6892-1. Metallic materials-Tensile testing-Part 1: Method of test at room temperature. International Organization for Standardization 2009.
- [34] Dubina D, Ungureanu V. Effect of imperfections on numerical simulation of instability behaviour of cold-formed steel members. *Thin Wall Struct* 2002;40:239-62.
- [35] Standard B. Specification for surface plates BS817. 2008.
- [36] Rasmussen K, Hancock G. Design of cold-formed stainless steel tubular members. II: Beams. *Journal of Structural Engineering* 1993;119:2368-86.
- [37] Yener M, Pekoz T. Partial moment redistribution in cold-formed steel. *Journal of Structural Engineering* 1985;111:1187-203.
- [38] Yener M, Pekoz T. Partial stress redistribution in cold-formed steel. *Journal of Structural Engineering* 1985;111:1169-86.
- [39] Shifferaw Y, Schafer B. Inelastic bending capacity of cold-formed steel members. *Journal of Structural Engineering* 2012;138:468-80.
- [40] Hui C, Gardner L, Nethercot DA. Moment redistribution in cold-formed steel continuous beams. *Thin Wall Struct* 2016;98:465-77.
- [41] Haidarali MR, Nethercot DA. Finite element modelling of cold-formed steel beams under local buckling or combined local/distortional buckling. *Thin Wall Struct* 2011;49:1554-62.